Pure and Applied Geophysics

The Mutual Response of the Tropical Squall Line and the Ocean

Xiaodong Hong,[1] Sethu Raman,[2] Richard M. Hodur[3] and Liang Xu[4]

Abstract—The Coupled Ocean/Atmosphere Mesoscale Prediction System (COAMPS) is used to investigate the mutual response of a tropical squall line and the ocean. Simulated squall line compares well with the observations, and consists of counterrotating vortices, and has a bow shape bulge toward the leading edge. In addition to these features, which are also shown in the previous numerical simulations, the unique results from the coupled simulation indicate that the air–sea interaction processes within the squall line are important. They affect both the atmosphere and the ocean locally. Simulated upper ocean displays significant response to the squall line with upwelling and baroclinicity. Depth of the ocean mixed layer in the coupled simulation becomes modified due to feedback processes. Ocean temperature acts as a destabilizing factor, and the salinity as a stabilizing factor. Surface turbulent fluxes from the coupled simulation are about 10% less than that of the uncoupled simulation. The SST in the coupled simulation decreases by about 0.21°C. Predicted squall line in the coupled simulation is weaker as compared to the uncoupled simulation. This is reflected in terms of differences in surface fluxes, cloud water, rain water and vertical velocities between the two simulations.

Key words: COAMPS, coupled model, mutual response, tropical squall line, atmosphere, ocean, heat fluxes.

1. Introduction

One of the scientific goals of the TOGA COARE (Tropical Ocean–Global Atmosphere, Coupled Ocean–Atmosphere Response Experiment) is to describe and understand the principal processes responsible for the coupling of the ocean and the atmosphere in the western Pacific warm-pool region (Webster and Lukas, 1992). The warm pool is a product of the interaction between the ocean and the atmosphere. There are many scales and forms of convection over this warm pool. The deep cumulus convection that occurs over this pool is important in maintaining

[1] University Corporation for Atmospheric Research, Naval Research Laboratory, Monterey, CA 93943, U.S.A.
[2] Department of Marine, Earth and Atmospheric Sciences, North Carolina State University, Raleigh, NC 27695, U.S.A.
[3] Naval Research Laboratory, Monterey, CA 93943, U.S.A.
[4] Science Applications International Corporation, Naval Research Laboratory, Monterey, CA 93943, U.S.A.

the heat and moisture balance in the tropical atmosphere, by transporting the fluxes of heat and moisture between the ocean and the atmosphere. It also can dominate the quantification of interfacial and related boundary-layer fluxes by cooling the ocean surface and transporting strong momentum and dry air to the surface. The convective processes in the squall line system produce precipitation which changes the upper ocean salinity, which in turn may exert a control on the ocean mixed-layer heat budget, and thus on the flux of heat to the atmosphere.

The squall line is an important precipitation system that occurs frequently over the TOGA COARE region. It is a sharply defined convective line with trailing stratiform precipitation in a mesoscale convective system. The 22 February, 1993 TOGA COARE squall line was a rapidly eastward propagating, north–south oriented large tropical convective line near Guadalcanal Island. This squall line has been investigated observationally by JORGENSEN *et al.* (1994, 1995, 1997), LEMONE *et al.* (1994) and numerically by TRIER *et al.* (1996, 1997). JORGENSEN *et al.* (1994, 1995, 1997) presented the general structure and momentum fluxes within the squall line system as well as the evolution of the line using data obtained by multiple airborne Doppler radars. LEMONE *et al.* (1994) characterized this squall line as a shear-perpendicular line since it oriented perpendicular to the low-level wind shear (from 800 mb to surface). They demonstrated that this shear-perpendicular line enhanced the east–west stress more than a shear-parallel line because downward transport of high u momentum was reinforced by u momentum generation in the rear inflow jet. Convective system increased surface stress and provided the largest eastward-directed stresses since it was an eastward-moving shear-perpendicular line. TRIER *et al.* (1996) indicated that the squall-line-induced surface fluxes could influence the strength and, more dramatically, the areal extent of the surface cold pool in the squall line system. Significant impact of squall-line-induced surface fluxes on the evolving deep convection at the leading edge of the cold pool is restricted to the later stages ($t \geq 4$ h) of simulations and is most substantial in regions where the ground-relative winds are strong and the convectively induced cold pool is initially weak and shallow. TRIER *et al.* (1997) further investigated the mechanisms responsible for meso- and convective-scale organization of the squall line system, using the same three-dimensional numerical cloud model as they utilized in the previous study.

As a strong coupling system over TOGA COARE warm pool region, the air–sea interaction processes associated with the squall line are important and must be understood. To investigate the mutual response of the squall line and the ocean, a coupled atmosphere and ocean mesoscale model is requested. In this paper we use the Coupled Ocean/Atmosphere Mesoscale Prediction System (COAMPS) (HODUR, 1993, 1997; XU, 1995) to simulate this squall line. We will also study the means by which the ocean cooling mechanism effects the squall line system and how the ocean responds to this convective system. Two basic numerical experiments were performed to achieve the above objectives: (i) simulation with the

atmospheric model only and (ii) simulation with the coupling between the atmosphere and the ocean.

2. The Coupled System

The numerical models used in this study are the Coupled Ocean/Atmosphere Mesoscale Prediction System (COAMPS) that consists of a nonhydrostatic primitive equation atmospheric model and a hydrostatic primitive equation ocean model as described by HODUR (1993, 1997). The topography implementation for the COAMPS atmospheric model is presented in detail by XU (1995). In the following we give only a brief description of COAMPS.

2.1. The Numerical Models

The COAMPS atmospheric model is comprised of the nonhydrostatic, compressible form of the dynamics (KLEMP and WILHELMSON, 1978) and parameterizations for subgrid-scale mixing (DEARDORFF, 1980), surface fluxes (LOUIS et al., 1982), explicit moist physics (RUTLEDGE and HOBBS, 1983), cumulus convective processes (KAIN, 1990; KAIN and FRITSCH, 1993), and radiation (HARSHVARDAN et al., 1987). The complete set of the prognostic equations can be found in HODUR (1997).

The moist physics applied here is the RUTLEDGE and HOBBS (1983) explicit treatment of the moist physics for both the nonconvective and convective clouds and precipitation. COAMPS performs as a cloud model in this study. The lateral boundary conditions for idealized simulations can be fixed, periodic, or radiation type similar to that proposed by ORLANSKI (1976). For the radiation conditions, all boundary values are set to their initial values at inflow points. At outflow points, the normal velocity, v_n, is computed using upstream differencing,

$$\frac{\partial v_n}{\partial t} = -(v_n + c_*)\frac{\partial v_n}{\partial n} \tag{1}$$

where v_n represents the velocity normal to the boundary and c_* is an estimate of the fastest-moving gravity wave directed out of the domain. The value of c_* can be specified as a constant or computed following the method described by MILLER and THORPE (1981). All other variables, other than v_n are linearly extrapolated to the boundary on outflow.

The subgrid-scale mixing in the COAMPS atmospheric model is treated following MELLOR and YAMADA (1974). The lower boundary conditions on the vertical mixing term are:

$$-\overline{(u'w')} = u_*^2 \frac{u}{|V|} \qquad (2)$$

$$-\overline{(v'w')} = u_*^2 \frac{v}{|V|} \qquad (3)$$

$$-\overline{(w'\theta')} = u_* \theta_* \qquad (4)$$

$$-\overline{(w'q_v')} = u_* q_{v*} \qquad (5)$$

where

$$|V| = (u^2 + v^2)^{1/2} \qquad (6)$$

at the first grid height above the surface; u, v and w are the wind components in the x, y and z directions, respectively; and u_*, θ_* and q_{v*} are velocity, potential temperature and mixing ratio scale values. At the upper boundary, the normal gradient of the vertical mixing terms is assumed to vanish, to prevent the development of unrealistic tendencies.

The COAMPS ocean model is capable of representing the deep (barotropic) response in the ocean, as well as to resolve the mixing processes within the mixed layer. The incompressible, hydrostatic equations similar to those described by CHANG (1985) are used with two modifications. First, the axisymmetric form of the equations is extended to three dimensions. Second, the predictive equation for the density is replaced with predictive equations for temperature and salinity, and the equation of state (GILL, 1982) is used to diagnose the density from the temperature, salinity and pressure. The complete set of equations for the ocean model has been described in HODUR (1997).

The subgrid-scale mixing in the COAMPS ocean model is similar to that used in the FNMOC Thermodynamical Ocean Prediction System (TOPS, CLANCY and MARTIN, 1981; CLANCY and POLLACK, 1983) and is based on the level-2 turbulence closure of MELLOR and YAMADA (1974). The upper boundary conditions on the vertical mixing terms are

$$-\overline{(u'w')} = \left(\frac{\rho_a}{\rho_o}\right) u_*^2 \frac{u}{|V|} \qquad (7)$$

$$-\overline{(v'w')} = \left(\frac{\rho_a}{\rho_o}\right) u_*^2 \frac{v}{|V|} \qquad (8)$$

$$-\overline{(w'T')} = -\left(\frac{\rho_a}{\rho_o C_{op}}\right) (C_p u_* T_* + L_v u_* q_*) \qquad (9)$$

$$-\overline{(w'S')} = \left(\frac{\rho_a}{\rho_o}\right) (u_* q_* S - P) \qquad (10)$$

where u, v and w are the ocean current speeds in the x, y and z directions, $|V|$ is defined as (6), u_*, T_* and q_* are the scale values of velocity, temperature, and water

vapor, S and T are the ocean temperature and the salinity, ρ_a and ρ_o are the densities at the air–ocean interface of the atmosphere and ocean, respectively, C_{op} is the specific heat at constant pressure for the ocean and P is the precipitation rate at the surface. At the lower boundary, the normal gradient of the vertical mixing terms is assumed to vanish, to prevent unrealistic tendencies from developing there.

The surface frictional velocity u_*, potential temperature θ_* and humidity q_* used in the estimates of fluxes (LOUIS *et al.*, 1982) are computed across the interface as:

$$u_* = \left(u^2 f_m \left(\frac{z}{z_0}, R_i \right) \right)^{(1/2)}, \quad \text{where} \quad u = \sqrt{(u_a - u_o)^2 + (v_a - v_o)^2}, \tag{11}$$

$$\theta_* = \frac{u(\theta_o - \theta_a) f_h \left(\dfrac{z}{z_0}, R_i \right)}{r u_*}, \tag{12}$$

and

$$q_* = \frac{u(q_{vo} - q_{va}) f_h \left(\dfrac{z}{z_0}, R_i \right)}{(r u_*)}. \tag{13}$$

In the above, subscripts "a" denote quantities at the lowest model level in the atmosphere (~ 5 m); subscripts "o", quantities at the uppermost level in the ocean (~ -2.5 m). f_m and f_h are stability functions of gradient Richardson number R_i and surface roughness z_0. The Charnock equation is used to estimate z_0. The latent heat for evaporation is assumed to come from the ocean surface layer. In addition, the precipitation contributes to the ocean as a source of fresh water at the same temperature of the SST and a sink to the salinity.

The lateral boundary conditions in the ocean model are similar to those used in the atmospheric model. Fixed-, periodic-, or radiation-type boundary conditions can be utilized. When using the radiative boundary conditions, all boundary values are set to their initial values for inflow points. At outflow points, (1) is used to predict the normal velocity component, while all other variables are linearly extrapolated to the boundary. The value of c_* is fixed at 10 m s^{-1}.

2.2. The Coupling Mechanisms

The COAMPS atmospheric model and ocean model can be integrated simultaneously or used as a stand-alone atmosphere or ocean forecast model. For a coupled integration, the surface fluxes of momentum, heat and moisture are exchanged across the air–sea interface at each ocean time step, since typically the ocean time step is considerably larger than the atmospheric time step. The fluxes of heat, moisture, momentum and moisture are averaged over all atmospheric time

steps during one ocean time step. These averaged fluxes are then used as the upper boundary condition in the ocean model. Also, the total precipitation is summed over all atmospheric time steps during one ocean time step. This total precipitation is then incorporated into the ocean model as a source of freshwater. The temperature of the upper level of the ocean model is fixed as the SST during all atmospheric time steps within any one ocean time step. Ocean provides SST and current speed in the first level for the lower boundary condition of atmosphere.

3. Observations

The tropical squall line simulated in this study occurred on 22 February, 1993 over TOGA/COARE area and was documented from the observations by JORGENSEN *et al.* (1994, 1995, 1997). Two NOAA P-3 aircrafts intercepted this rapidly eastward propagating north–south oriented convective line near Guadalcanal Island. The environment was characterized by moderate instability. Convective Available Potential Energy (CAPE) was $1442 \, \text{J kg}^{-1}$. A moderate low-level wind shear was present. Shear in horizontal (east–west) wind difference from 800 mb to the surface was about $13 \, \text{m s}^{-1}$. The convective system was about 100 km long, oriented perpendicular to the low-level shear and located at the leading edge (east side) of a large-scale westerly wind event. The squall line initially was highly linear, although later developed a pronounced "bow-shaped" bulge in the leading convective line in about 1.5 hours (JORGENSEN *et al.*, 1997). The bowed line moved east at about $12 \, \text{m s}^{-1}$. Associated with the eastward "bow" was counter-rotating vortices: the anticyclonic or counterclockwise on the northern or equatorward end of the line and the cyclonic or clockwise on the south or poleward end of the line. The anticyclonic circulation at the northern end of the line developed in a region of enhanced westerly "rear inflow" and was most pronounced at low levels where the environmental wind shear was the largest. The cyclonic circulation at the southern end of the line may have amplified into a tropical cyclone over the next several days. These counter-rotating "bookend" vortices are common circulation features associated with the squall line bowing (WEISMAN *et al.*, 1988). They may be initiated by both the tilting of the ambient horizontal vorticity and the tilting of the westerly mesoscale rear-inflow (JORGENSEN and SMULL, 1993; DAVIS and WEISMAN, 1994). A low-level "gust-front" was associated with the convective leading edge, with an equivalent potential temperature decrease of about 15°K across the leading edge. An updraft with a maximum vertical velocity (w) of $4-5 \, \text{m s}^{-1}$ was observed at low altitudes near the leading edge. A secondary maximum of $8-10 \, \text{m s}^{-1}$ in w was observed at a height of 10 km (JORGENSEN *et al.*, 1994).

4. Model Domain and Initial Conditions

Model domain is $120 \times 120 \times 17.8$ km with 61×61 grid points in the horizontal and 50 in the vertical. It includes 30 layers in the atmosphere and 20 layers in the ocean. A resolution of 2 km is used in the horizontal and a stretched resolution in the vertical, from 125 m in the lowest layer to 1000 m in the upper levels. This horizontal resolution was used to suit the available computer resources that would allow a large enough physical domain necessary for the complete squall line simulation. A time-splitting procedure is employed to improve the computational efficiency in solving the compressible equations. A speed of $12 \mathrm{~m~s}^{-1}$ has been set in the simulation for the squall line motion. For the atmospheric model, the large time step is 6 seconds and the small time step 0.6 seconds. For the ocean model, the large time step is 240 seconds and the small time step 6 seconds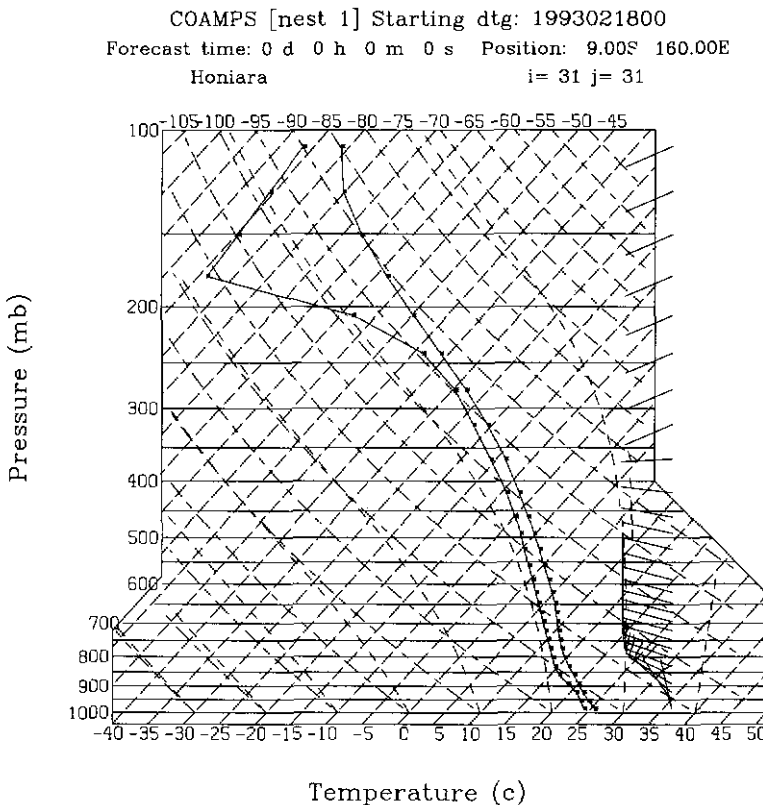. Initial thermodynamic field and wind field use the composite sounding derived from P-3 flight level data and rawinsonde data at Honiara, Guadalcanal ($\sim 9°$S, $160°$E) at 1800 UTC on 22 February, 1993 adapted from TRIER et al. (1996) (Fig. 1). Initial thermal perturbation was oriented with a radius of 20 km in the along-line direction, and 5 km in the perpendicular direction, and 1600 m in the vertical. The maximum magnitude of thermal is $2°$K at the center, decreasing to $0°$K at the edges. The initial thermal perturbation form followed the one given by KLEMP and WILHELM-SON (1978). It is believed that this initial thermal perturbation mechanism is too weak to affect subsequent squall line behavior. The SST is set to a constant value throughout the simulation for the uncoupled case. A rigid wall boundary condition is specified at the upper boundary. This constraint should be reasonable if that boundary remains at a sufficient distance above cloud-top level and if vertical transport of horizontal momentum by gravity waves is considered unimportant. Radiation conditions are used for the lateral boundaries.

For the coupled simulation, initial current is assumed zero. The thermal profiles that include temperature and salinity variations have used CTD data from the R/V Le Noroit (Fig. 2). Observations were made with a SeaBird SBE-9 probe and were processed to a 2-dbar vertical resolution. The data set used here was obtained at 1810 UTC on 22 February, 1993 at $2°$S and $156°$E. The pressure in dbars has been converted to depth in meters following a method suggested by SAUNDERS and FOFONOFF (1976). First layer of temperature has been used for the initial SST field.

5. Discussion of Results

The 22 February, 1993 TOGA COARE squall line studied in this paper has been numerically investigated by TRIER et al. (1996, 1997). The sensitivity of the simulated squall line to the surface heat fluxes and ice microphysics indicated that the small-scale physical processes are important. Mechanisms responsible for meso-

and convective-scale organization within the simulated squall line also have been
given in their paper. In this paper, we will focus on the ocean effect on the squall
line and the ocean response to the squall line.

5.1. *General Structure and Evolution of the Simulated Squall Line*

General structure and evolution of the simulated squall line will be given here
before we further discuss the ocean effect and the ocean response. The following
results are based on the uncoupled simulation.

(1) Horizontal structure and evolution

Radar reflectivity and flow vectors at 1000 m (above ground level) at 2 h, 3 h and
4 h are shown in Figures 3a, b and c, respectively. Radar reflectivity is calculated

COAMPS [nest 1] Starting dtg: 1993021800
Forecast time: 0 d 0 h 0 m 0 s   Position: 9.00S 160.00E
Honiara   i= 31 j= 31

Temperature (c)

Figure 1
Initial thermodynamic and wind field for the atmosphere based on a composite sounding derived from
P-3 flight level data and rawinsonde data at Honiara, Guadalcanal at 1800 UTC on February, 1993.
Each short barb represents 5 m s^{-1}, while each long barb represents 10 m s^{-1}.
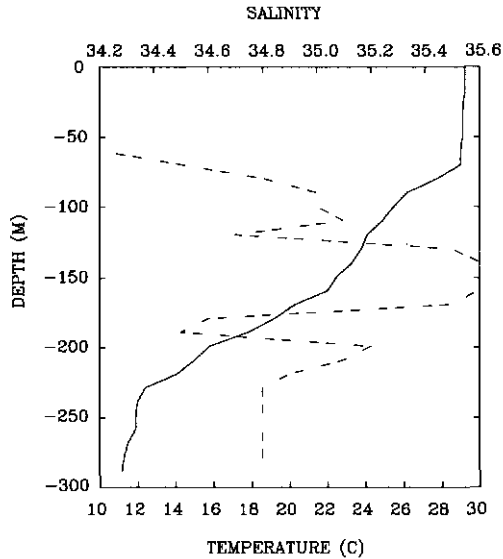
SALINITY

Figure 2

Initial temperature (°C) and salinity (ppt) for the ocean based on the CTD data obtained from the R/V Le Noroit made with a SeaBird SBE-9 probe and processed to a 2-dbar vertical resolution at 1810 UTC on February, 1993. The solid line represents temperature and the dashed line represents salinity.

from water and ice as in SMITH *et al.* (1975). Only a subdomain, 8 to 88 km in x direction and 18 to 98 in y direction respectively, is shown to illustrate important features. The bow shape has begun to form in the southern part of the squall line at 2 h (Fig. 3a), with a weaker line in the northern portion of the system. The flow diverges behind the leading edge of the bowlike feature, with a strong northerly wind in the northern portion of the system. The system continues to expand in size in the next hour as shown in Figure 3b. At a later time, the flow develops into a cyclonic vortex and the bow shape becomes more prominent in the southern part of the squall line (Figs. 3b,c). Northerly wind in the northern part of the system has changed into a anticyclonic circulation. The counter-rotating vortices compare well with the observations as shown in JORGENSEN *et al.* (1997). A strong rear inflow jet forms between these counter-rotating vortex circulations, resulting in the bow-shape bulge toward the leading edge of the system (DAVIS and WEISMAN, 1994). Convection and hence the radar reflectivity is more widespread at this time although the magnitude has not increased significantly.

There are strong updrafts along the leading edge of the system and downdrafts in the rear side of the system as indicated in Figures 4a,b,c, which show the vertical velocity in countours and accumulated rainfall in gray scale at 1000 m above the surface at 2 h, 3 h and 4 h, respectively. The maximum vertical velocity reaches 3.81 m s^{-1} at this level in Figure 4a. Stronger updrafts occur in the southern part
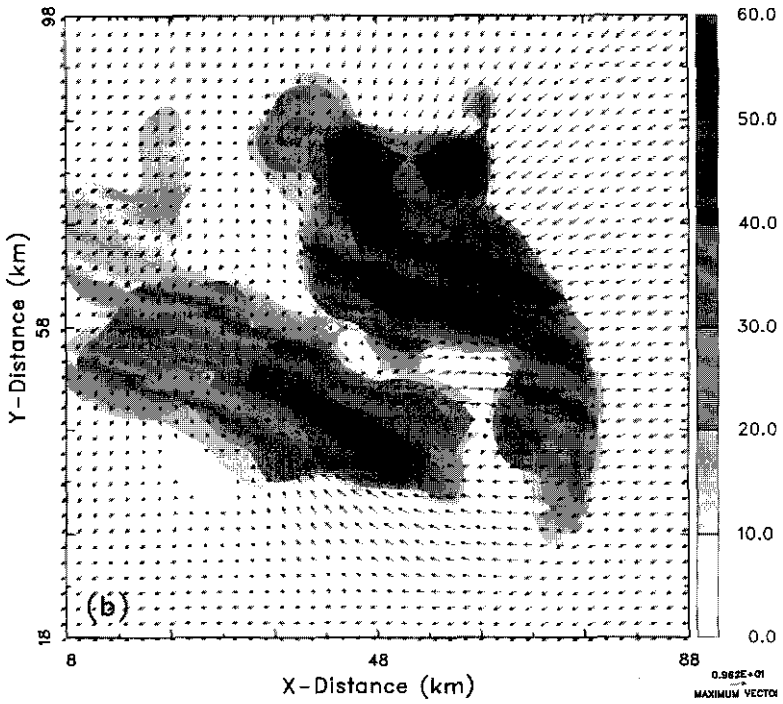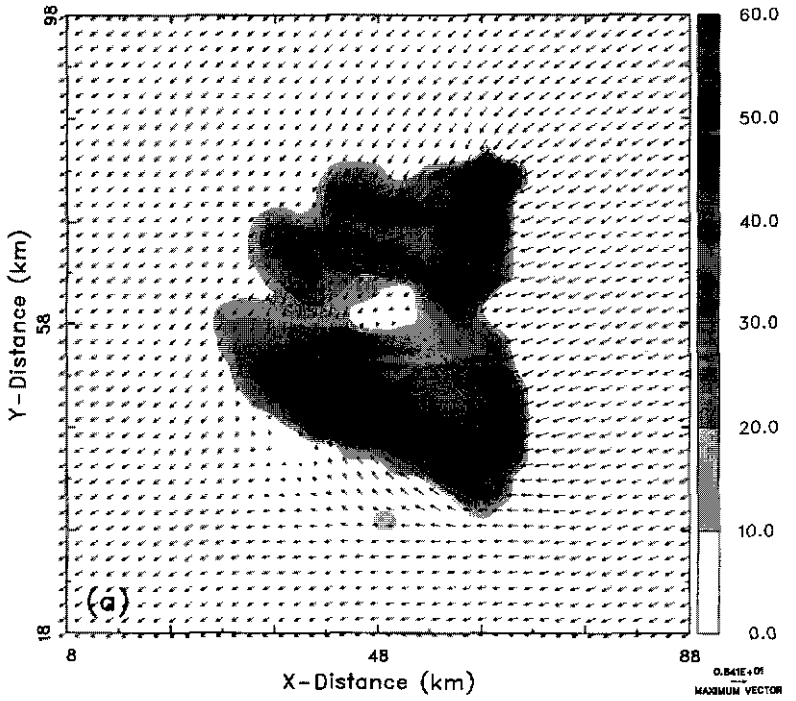
Figs. 3 a,b

Figure 3
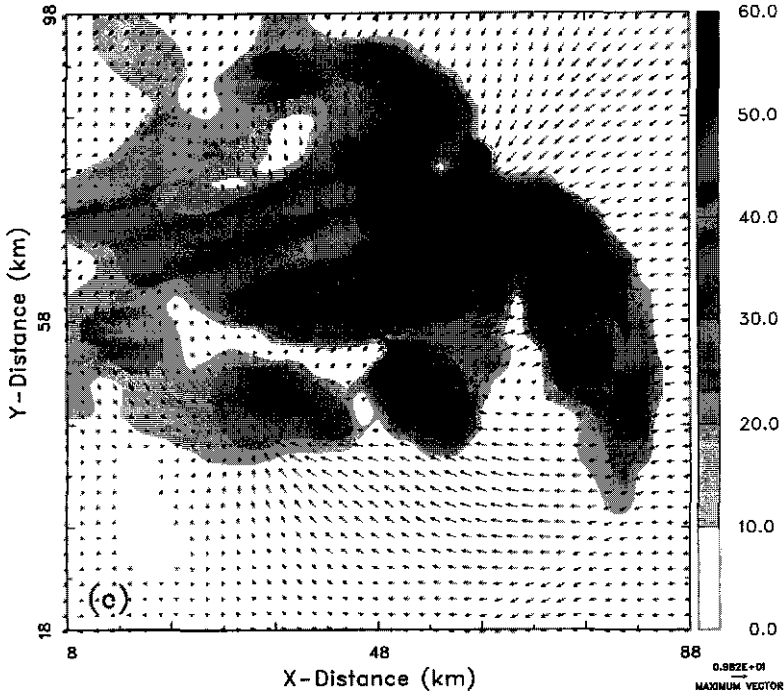Model-predicted radar reflectivity (dBz) in gray scale and flow vectors (m s^{-1}) at 1000 m (above ground level) at (a) 2 h, (b) 3 h and (c) 4 h. Only a subdomain, 8 to 88 km in x direction and 18 to 98 km in y directions, is shown to emphasize important features.

of the squall line as strong convergence develops in this region in conjunction with the cyclonic or clockwise vortex. Rainfall occurs at the downdraft location with a magnitude of about 10 cm (Fig. 4b). Heavier rainfall occurs in the southern part of the system because of the existence of stronger updrafts in the southern part of the leading edge. Rainfall becomes less asymmetric after 3 h. This is apparent from Figure 4c, which exhibits the same variables as indicated in Figure 4a except for 4 h. The presence of two almost equal rainfall areas indicates that the system is approximately symmetric with reference to the rear inflow jet. The positions of the rainfall maxima and the negative vertical velocity maxima are matched.

The predicted system has features closer to the observations at 4 h as evidenced in Figures 3c and 4c. The area of rear inflow jet increases significantly with a large bow-shape bulge for both the simulation (Figs. 3c and 4c) and the observation (JORGENSEN et al., 1997). The cyclonic circulation in the southern end of the squall line has increased during this time and may have led to the development of a tropical cyclone over the next several days as indicated by JORGENSEN et al. (1994). The upward motions are stronger than before with a maximum of 4.5 m s^{-1} near
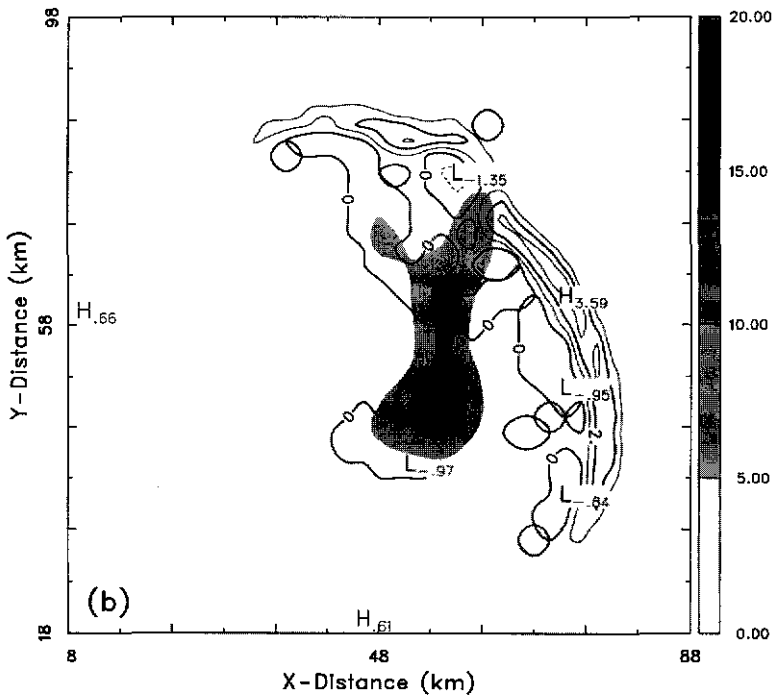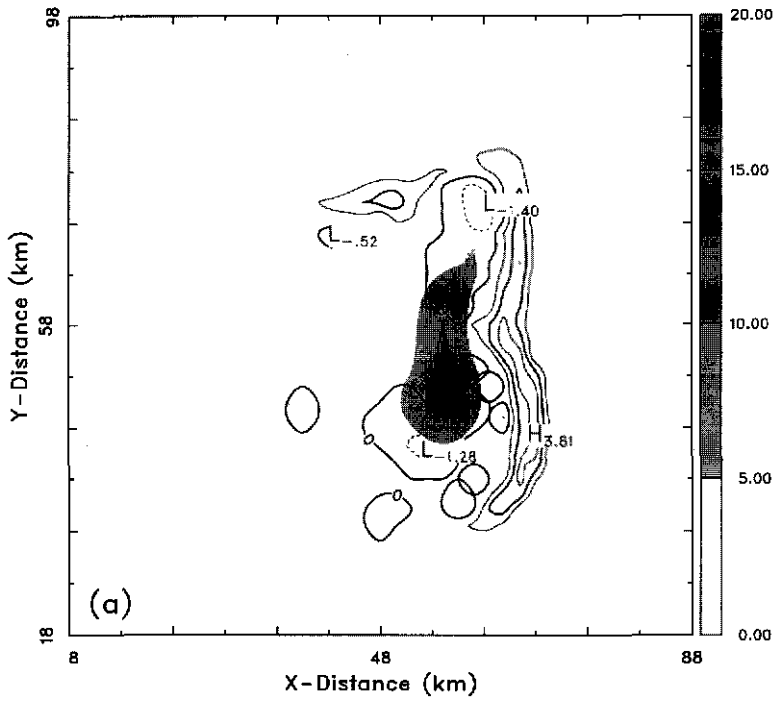
Figs. 4 a,b
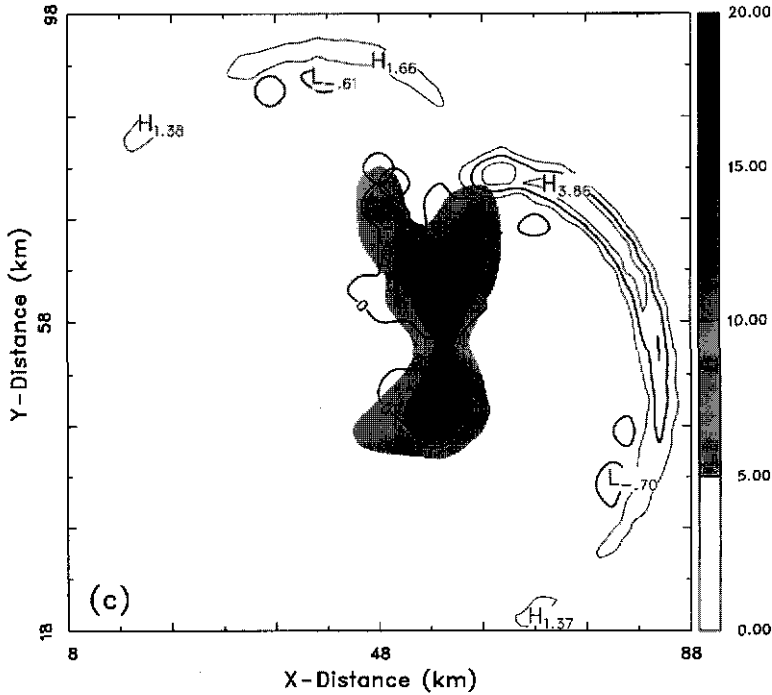
Figure 4
The vertical velocity (m s^{-1}) in contours and the rainfall (cm) in gray scale at 1000 m (above ground level) at (a) 2 h, (b) 3 h and (c) 4 h. The contour interval is 1.0 m s^{-1}.

the northern end of the leading edge. The downdrafts have also increased considerably with a minimum of -1.5 m s^{-1}, indicating increased rainfall. Increase in the rainfall area in the nothern part of the system is believed to have been caused by strong convection.

The perturbation pressure (mb) in contours and temperature change (°C) in gray scale in the first model level (125 m) at 2 h, 3 h and 4 h of the simulation is shown in Figures 5a,b,c, respectively. Downdrafts with precipitation from the convective clouds produce a cold pool with a maximum negative temperature anomaly of ~ 5°C and an associated meso-high with a maximum pressure perturbation of 1.0 mb (Fig. 5a). Occurrence of this cold pool emphasizes the importance of the cooling mechanism in determining the observed upper limit on SSTs. The cold pool is caused by explicit melting and evaporative cooling of air below the stratiform cloud, which eventually reaches the surface, by downdrafts. Although the temperature of the cold pool did not decrease, the area covered by negative temperature perturbation has increased at 3 h (Fig. 5b), and formed a large area of meso-high. The cold pool region is larger than the rainfall region in this simulation. It is believed that the colder air caused by evaporative cooling has spread over a

large area by divergent surface outflow. Two meso-highs located at the southern
and northern parts of the squall line are consistent with the centers of the two
downdrafts, two rainfall regions and two cold pools. At 4 h (Fig. 5c), a bow-shape
feature can be seen as the cold pool expands with small and narrow regions of
positive pressure perturbation directly behind the leading edge of the squall line.
These small and narrow regions of high pressure correspond to new downdrafts
which are accompanied by new developed updrafts.

(2) Vertical structure and evolution

Vertical cross sections of equivalent potential temperature θ_e and flow vectors
along the line $y = 37$ are delineated in Figures 6a (2 h), 6b (3 h) and 6c (4 h).
Rainfall produced from the initial updrafts generates a cold pool that spreads
against the surface inflow (Fig. 6a). The updraft originates in the surface layer
ahead of the system and is characterized by high values of θ_e, while the downdraft
is associated with the low θ_e air. The downdraft which begins at mid-levels brings
air with low θ_e down to the surface and causes air to spread towards the front of
the system. The cold pool triggers new updrafts in the lower layers and leads to
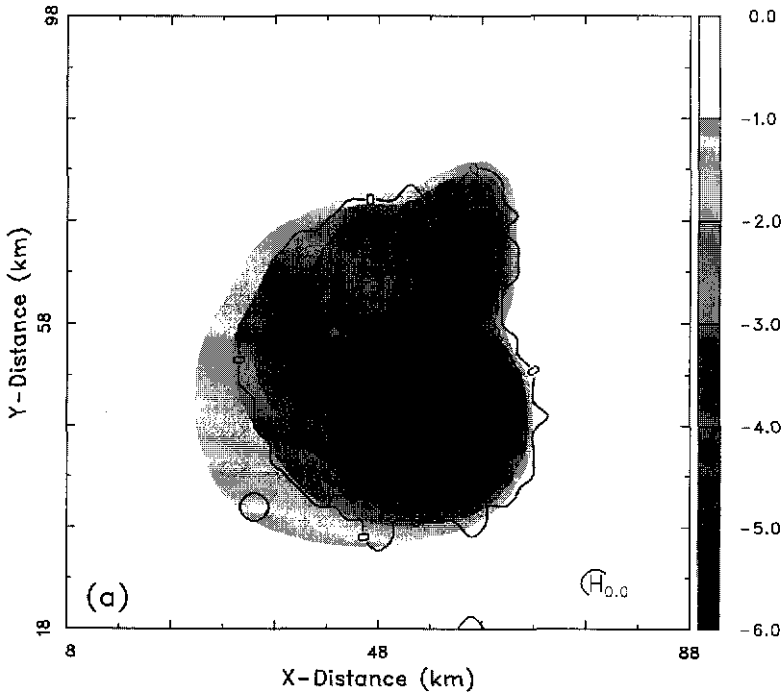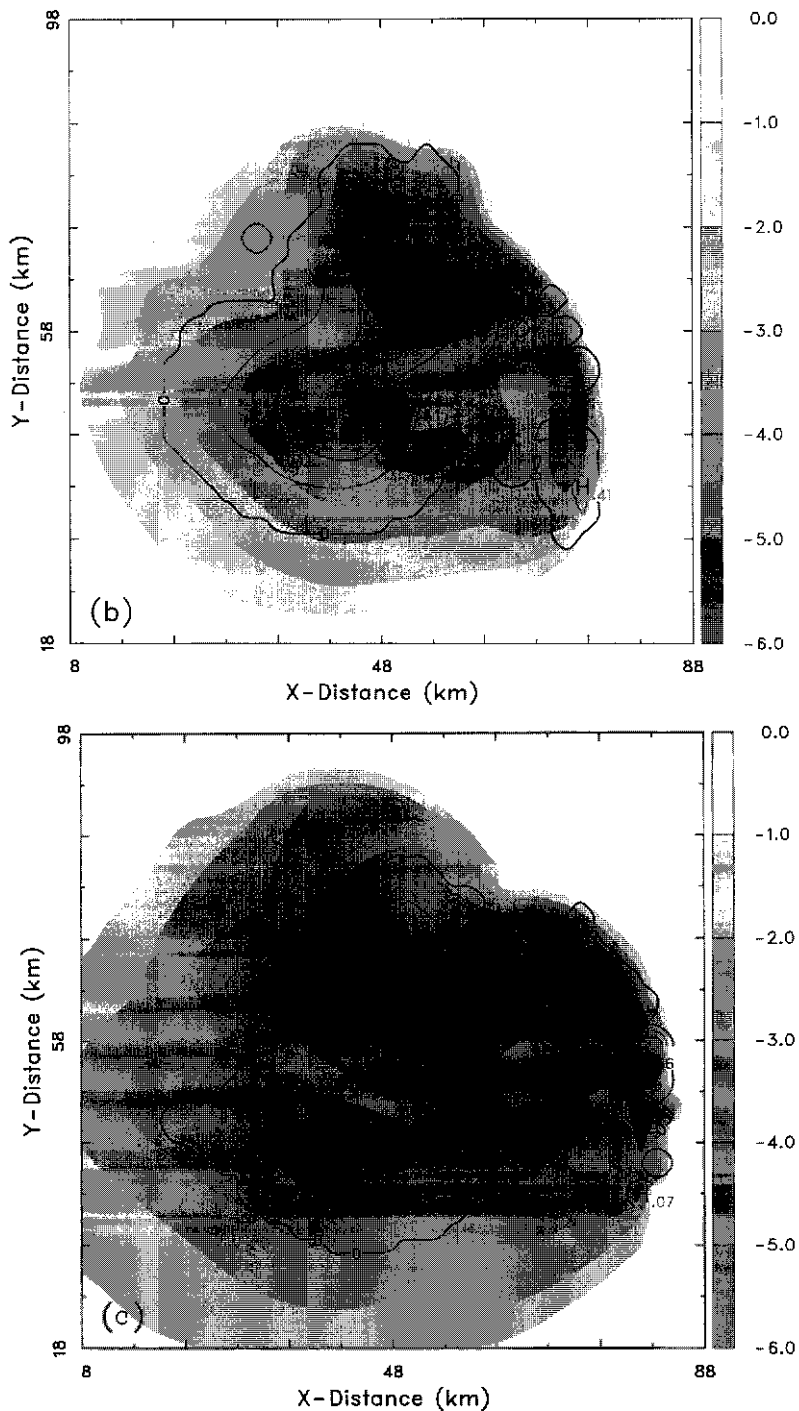

Figs. 5a

Figure 5
The perturbation pressure (mb) in contours and temperature change (°C) in gray scale in the first model
level (125 m) at (a) 2 h, (b) 3 h and (c) 4 h of the simulation. The contour interval is 0.2 mb.

rearward tilting of the θ_e field as shown in Figure 6b. Convergence of the inflows from the front and the rear of the system indicates the generation of new cells. At higher altitudes most of the updraft air turns abruptly.
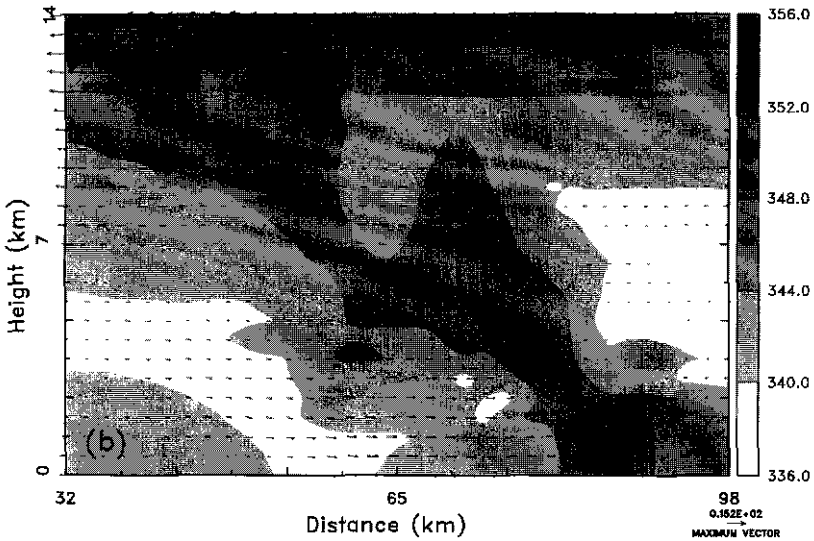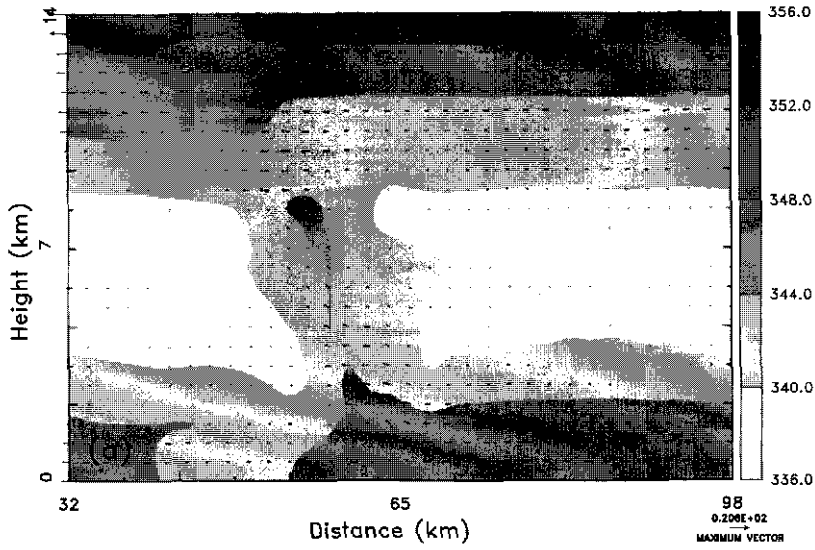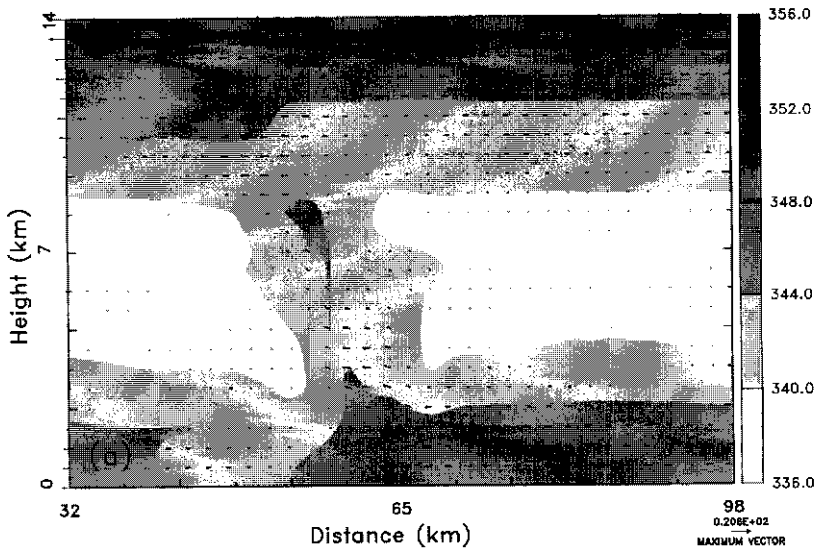

Figs. 6 a,b

Figure 6
The vertical cross sections of equivalent potential temperature (°C) in gray scale and flow vectors along
the line, $y = 37$ for (a) 2 h, (b) 3 h and (c) 4 h. Only a subdomain, 32 to 98 km in x direction and 0 to
14 km in z direction, is shown to emphasize important features.

High θ_e air from low levels transfers the moist energy into upper layers through
the rearward tilting inflow jet located at the front of the system. Existence of a
downdraft at this location causes low θ_e air to descend from the rear of the system
at 3 h (Fig. 6b). The rear inflow jet increases in intensity as it penetrates and
approaches the leading edge of the system. This causes the convective system to tilt
further towards the rearward direction.

According to WEISMAN (1993), it is during this rearward-tilting phase of the
system that a significant rear-inflow jet is typically generated. This occurs as the
buoyant plume aloft and cold pool near the surface generate horizontal vorticity,
thereby accelerating the flow from rear to front at mid-levels. This mechanism is
equivalent to a configuration in which a minimum in the buoyancy-derived pressure
field exists at mid-levels that accelerates the rear-inflow current.

This jet-like rear inflow begins at mid- or upper levels on the rear edge of the
stratiform rain area and descends toward the front of the system. JOHNSON and
HAMILTON (1988) and BRANDES (1990) described the structures of this rear inflow
and the associated surface wake lows in a squall line and a mesovortex, respectively.
The rear inflow not only moved with the squall line but also intruded farther into
the precipitation region. The rear inflow descends from mid-levels to lower levels in
the trailing stratiform region during the early stages of the squall line. Intrusion of
the dry mid-tropospheric inflow can be clearly seen in Figure 6c. Strong rear inflow
jet brings dry mid-level air to the surface and the system further tilts.

Thermodynamic properties of the squall line depend on the distribution of diabatic heating and evaporative cooling as shown in Figure 7. Diabatic heating in Figure 7 includes that due to condensation and evaporation. Evaporative cooling derives from the rainfall below the cloud layer. The vertical cross section of diabatic heating and evaporative cooling at 2 h (Fig. 7a) displays the tilting of the squall line, horizontal spreading of the air and vertical depth of the cold pool. The air beneath the squall line is strongly cooled by the heavy precipitation zone, which consequently produces a strong horizontal temperature gradient. Precipitation helps to maintain an intensified downdraft in the proximity of the updraft, which triggers new convective cells and contributes to further development of the squall line. Existence of a small diabatic heating center near the leading edge indicates the generation of a new cell beginning to form precipitation (this new cell as shown at a later time is presented in Fig. 7b). Warming results from dry adiabatic subsidence separates the evaporative cooling area in the rear from the main convective cells in the front. This leads to the decaying stage of the convective cell in the rear side due to the lack of energy sustenance.

A more widespread and intense cold pool is predicted at 4 h as shown in Figure 7b. The squall line has developed more closely to the east. Diabatic heating distribution also indicates that a new cell has been generated near the leading edge. Evaporative cooling in the rear side is stronger which means that the subsidence is more intense. Stronger subsidence decreases the pressure gradient and the rear inflow, which in turn reduces the potential for convective instability. This leads to a decrease in the intensity of the convective cell near the rear side of the squall line. On the other hand, stronger cold pool in the rear side contributes to the tilting of the squall line, which in turn can promote convective development through the enhancement of the vertical motion near the front of the system.

Cross sections of the east–west wind component in gray scale and vertical velocity in contours for 2 h and 4 h are shown in Figures 8a and b, respectively. Downdrafts separating the updrafts in Figure 8a are consistent with the distribution of evaporative cooling in Figure 7a. The downdraft in the lower level triggers a new convective cell in the leading edge of the squall line. This results in the tilting of the system in the rear direction of the squall line motion as a new convective cell forms. This rearward tilt has been observed according to JORGENSEN *et al.* (1995). The old convective cell at higher altitude tilts upwards and is beginning to reach the mature stage with a maximum vertical velocity of 3.97 m s^{-1}. The convective cell in the rear side of the system is in a decaying stage as the energy is dissipated. The downdrafts in the middle of the system triggers the development of a new cell near the leading edge; however, they cut off the energy supply for the cell in the rear side of the system. Convergence and divergence patterns can be inferred from the distribution of the east–west wind component. A region of strong convergence corresponds to the location of the mature convective cell at higher altitudes. A moderate convergence area in the lower altitudes corresponds to the new cell which developed near
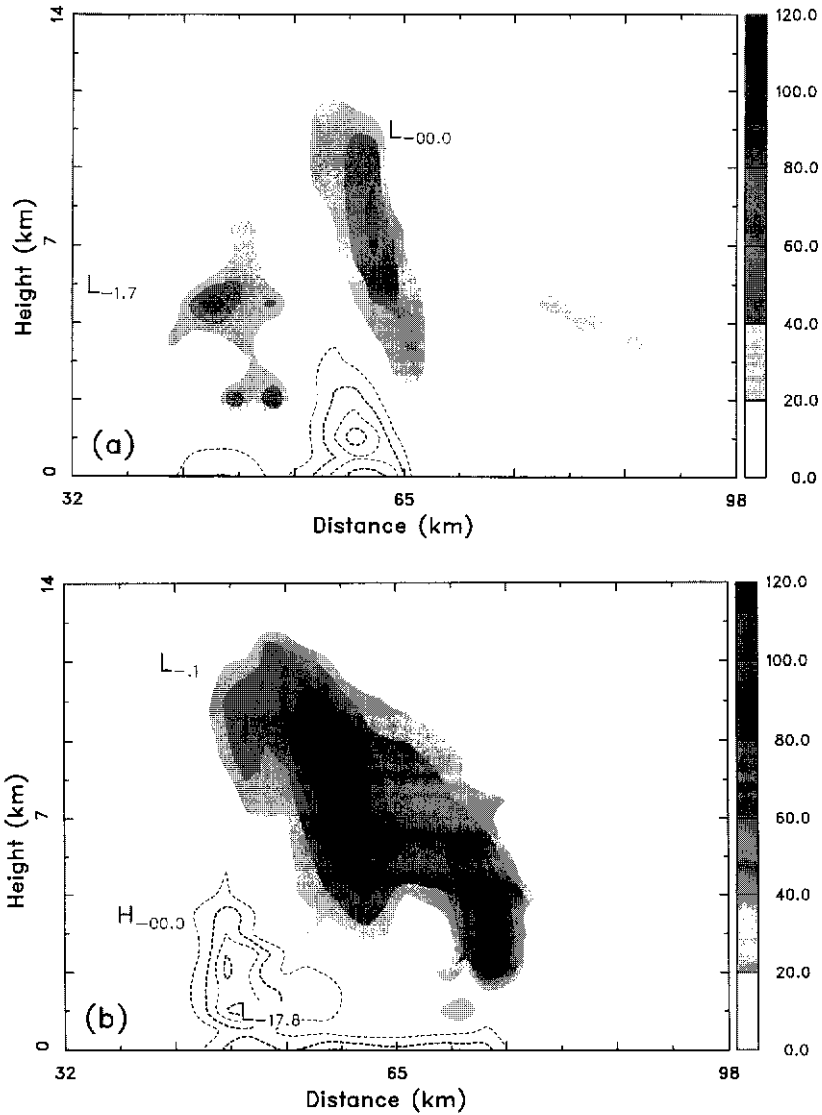
Figure 7

The vertical cross sections of diabatic heating (°C h^{-1}) in gray scale and evaporative cooling in contours (°C h^{-1}) along the line, $y = 37$ for (a) 2 h and (b) 4 h. The contour interval is -4.0°C and starts from 0.0°C. Only a subdomain, 32 to 98 km in x direction and 0 to 14 km in z direction, is shown to emphasize important features.

Figure 8
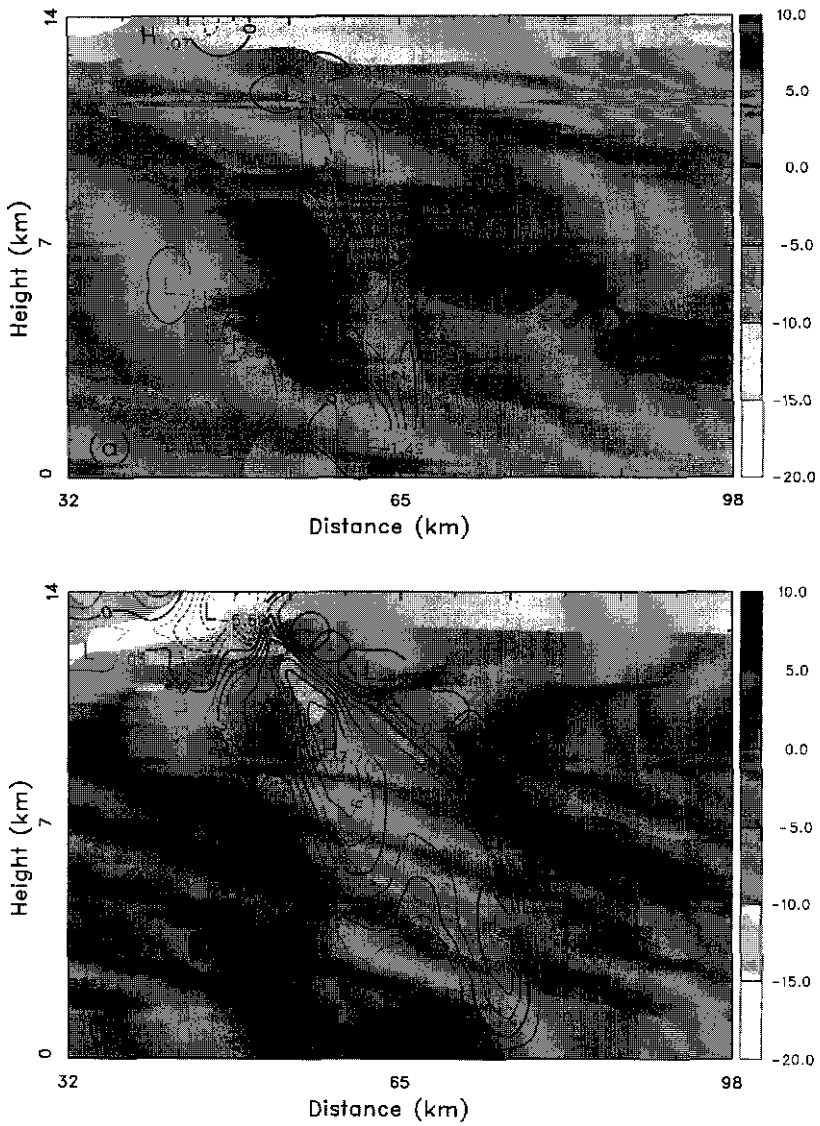The vertical cross section of east–west wind component (m s^{-1}) in gray scale and vertical velocity (m s^{-1}) in contours along the line, $y = 37$ for (a) 2 h and (b) 4 h. The contour interval is 1.0 m s^{-1}. Only a subdomain, 32 to 98 km in x direction and 0 to 14 km in z direction is shown to emphasize important features.

the leading edge of the squall line. Weak divergence in the rear side corresponds to the decay of the old cell.

A cross section of the predicted vertical velocities at 4 h in Figure 7b shows a very similar pattern to the observations as shown in JORGENSEN et al. (1994). The vertical cross section from the simulation is set as one by JORGENSEN et al. (1994), in which the rear inflow is large ($y = 37$ here). The system becomes wider in the horizontal direction and the leading edge is further to the east. Rearward tilting of the system is more obvious. The two updrafts discussed in Figure 8a have become stronger. One is at an altitude of about 4 km near the leading edge and the other is at approximately 10 km. The maximum wind speed in the lower level reaches a value of 4.86 m s^{-1}; and the upper level maximum is 7.77 m s^{-1}. These are close to observations: 4–5 m s^{-1} at lower levels near the leading edge and 8–10 m s^{-1} at 10 km (as shown in JORGENSEN et al., 1994).

Squall line usually includes a stratiform region in the rear side and a convective region near the leading edge. Rainfall characteristics and the flow patterns in each region are quite different. Figure 9 illustrates model-calculated radar reflectivity (dBz) in gray scale and the distribution of ice crystals (gkg^{-1}) in contours in the fully developed squall line at a simulation time of 5 h. The magnitude of the rainfall in the stratiform region is quite different from that over the convective region. This represents a common feature of the squall line, in which a marked unsaturated, warm mesoscale descent exists in the rear side beneath the stratiform region and
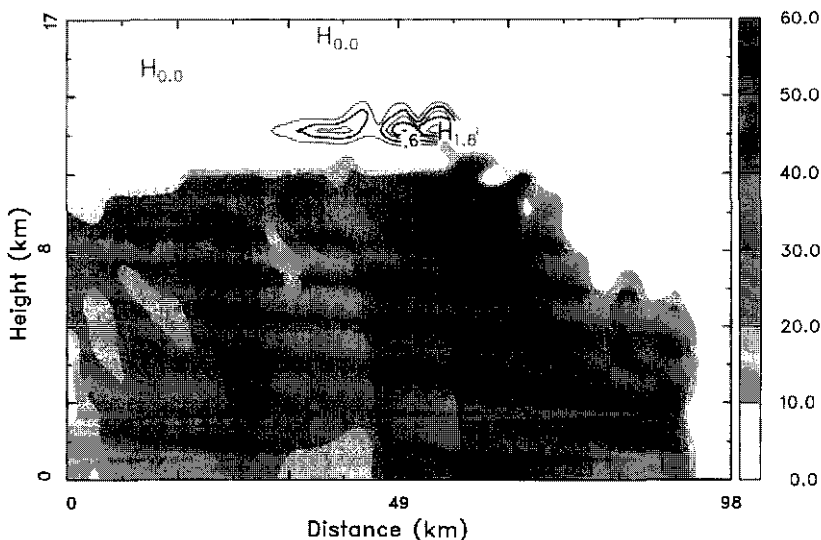

Figure 9
The vertical cross section of model-calculated radar reflectivity (dBz) in gray scale and the distribution of ice crystals (gkg^{-1}) in contours along the line, $y = 37$ for 5 h. The contour interval is 0.3 gkg^{-1}. A subdomain in x direction from 0 to 98 km is shown to emphasize important features.

cold, nearly saturated convective-scale downdrafts exist in the cold pool region. A small convective region in the leading edge represents a developing convective cell that will extend the system further east. A transition zone develops between the convective and stratiform regions, characterized by relatively small reflectivities at low altitudes. This region is associated mainly with a layer of downward motion. The transition zone separates the intense precipitation zone near the leading edge from the lighter, more uniform rainfall region in the rear.

5.2. Features from the Coupled Simulation

In this section the important features from the coupled simulation will be presented. We focus on the differences of surface heat fluxes, sea-surface temperature changes, ocean response to the squall line and the strength of the squall line system between the coupled and uncoupled simulations.

(1) Surface fluxes

With the coupled atmosphere–ocean model, the surface fluxes are different from uncoupled simulation because of the cooling of the ocean surface by precipitation, evaporation and ocean upwelling. Figure 10 is the variation of domain averaged latent heat flux (Watts m^{-2}) and sensible heat flux (Watts m^{-2}) with time. Solid line represents uncoupled simulation and dashed line coupled simulation. In the early stages, surface heat fluxes exhibit a small difference between the two simulations. After the occurrence of the precipitation, surface heat fluxes diminish in the coupled simulation. The SST held constant in the uncoupled simulation contributed to an overestimate of the surface heat fluxes by enhancing the vertical gradients of temperature and moisture. However, in a coupled model, deep convection decreases the sea-surface temperatures because of precipitation, evaporative cooling and ocean upwelling. Convective exchange of the heat and moisture with these modified surface conditions changes the vertical temperature profile in the atmosphere.

(2) Sea-surface temperature changes

The sea-surface temperature (SST) is assumed equal to the first layer of the ocean model and is predicted by the thermodynamic equation. The SST is very sensitive to changes in the state of the overlying atmosphere, and *vice versa*. There is a nonlinear relationship between the SST and latent heat flux, even when salinity effects are ignored. Figures 11a and b depict the horizontal cross sections of temperature change (°C) in gray scale and salinity change (ppt) in contours at an ocean depth of 2.5 m for 2 h and 4 h, respectively. At 2 h into the simulation, maximum SST change is about −0.1°C and occurs in the region of rainfall (as was shown in Fig. 4a). Fresh water also changes the salinity near the ocean surface, and the location of maximum salinity is close to the location of maximum rainfall (as was shown in Figs. 4a and 11a).
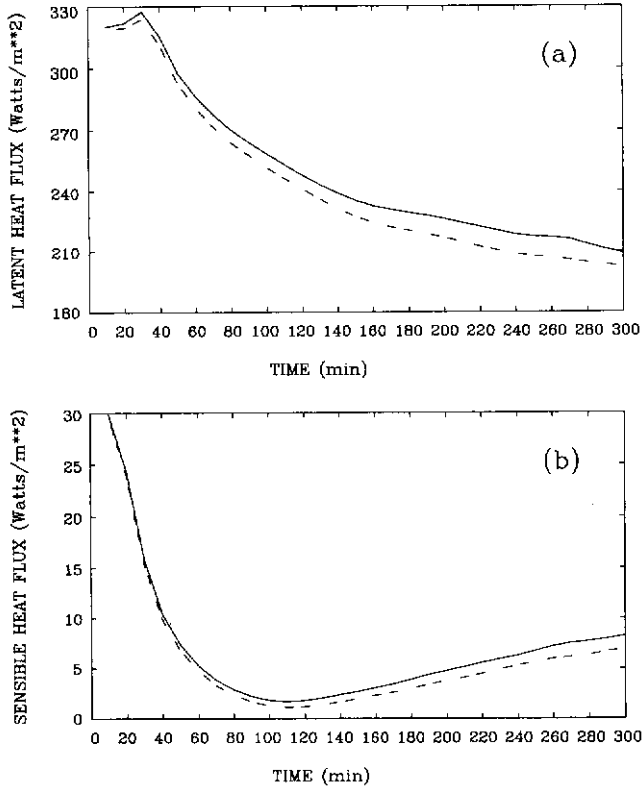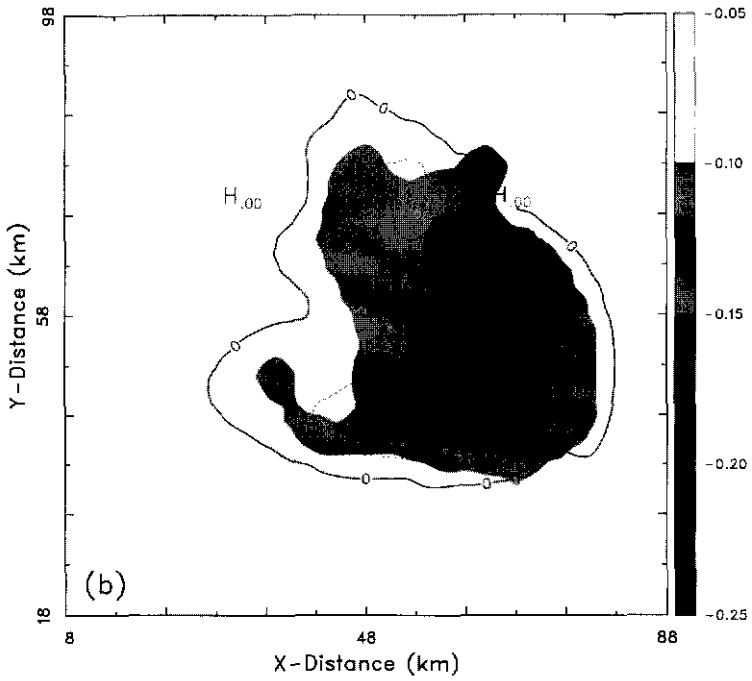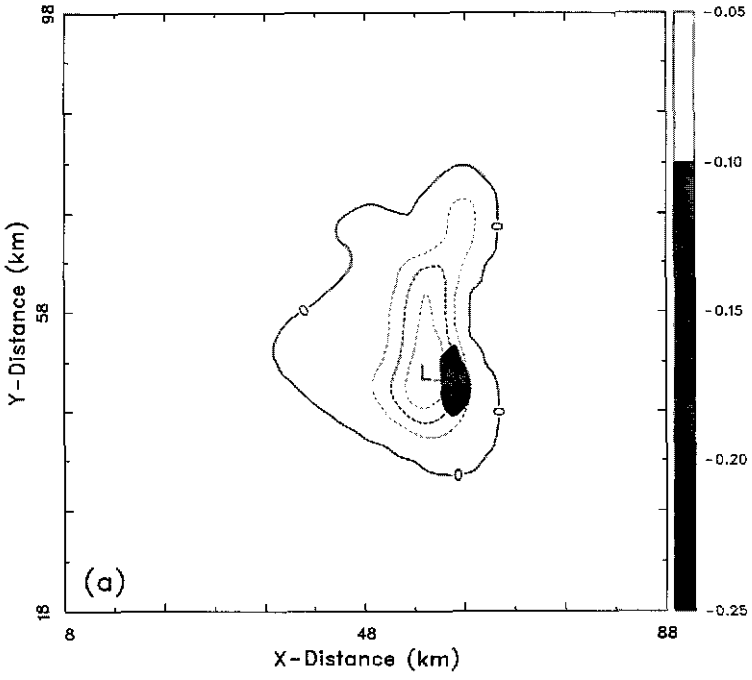
Figure 10

The time variation of domain averaged (a) latent heat flux (Watts m^{-2}) and (b) sensible heat flux (Watts m^{-2}). The solid line and dashed line represent the uncoupled and coupled simulation, respectively.

Sea-surface temperature (SST) decreases by 0.21°C at 4 h into the simulation (Fig. 11b). Deep convection in the squall line system decreases sea-surface temperature because of the precipitation, evaporation and ocean upwelling. The area of maximum temperature decrease corresponds to the rainfall area and the upwelling area (as will be shown in Fig. 13). More freshwater into the ocean decreases salinity and enlarges the area covered by freshwater.

(3) Ocean response

Once deep atmospheric convections develop, they represent an important forcing mechanism for the upper ocean. Oceanic response consists of dynamic effects and turbulent mixing associated with large momentum fluxes, as well as diabatic effects associated with altered buoyancy fluxes. Figures 12a and b picture the vertical cross sections of the east–west wind component (m s^{-1}) in gray scale and vertical velocity (m s^{-1}) in contours for the atmosphere in the coupled simulation for 2 h and 4 h, respectively. Figures 13a and b show the vertical cross sections of the east–west
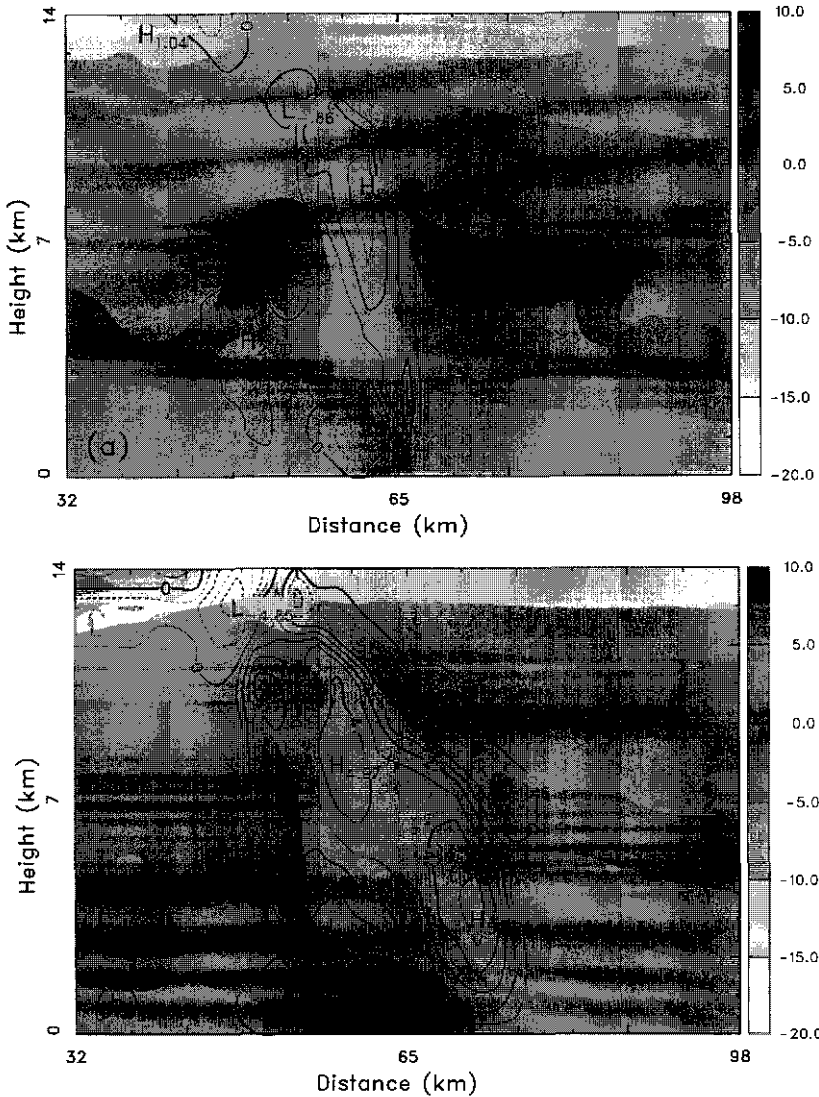
Figure 12

The vertical cross section of east–west wind component (m s^{-1}) in gray scale and vertical velocity (m s^{-1}) in contours along the line, $y = 37$ for the atmosphere in the coupled simulation for (a) 2 h and (b) 4 h. The contour interval is 1.0 m s^{-1}. Only a subdomain, 32 to 98 km in x direction and 0 to 14 km in z direction, is shown to emphasize important features.

Figure 11

The horizontal cross section of temperature change (°C) in gray scale and salinity change (ppt) in contours at the ocean depth of 2.5 m for (a) 2 h and (b) 4 h. The contour interval is 0.1 ppt. Only a subdomain, 8 to 98 km in both x and y directions, is shown to emphasize important features.
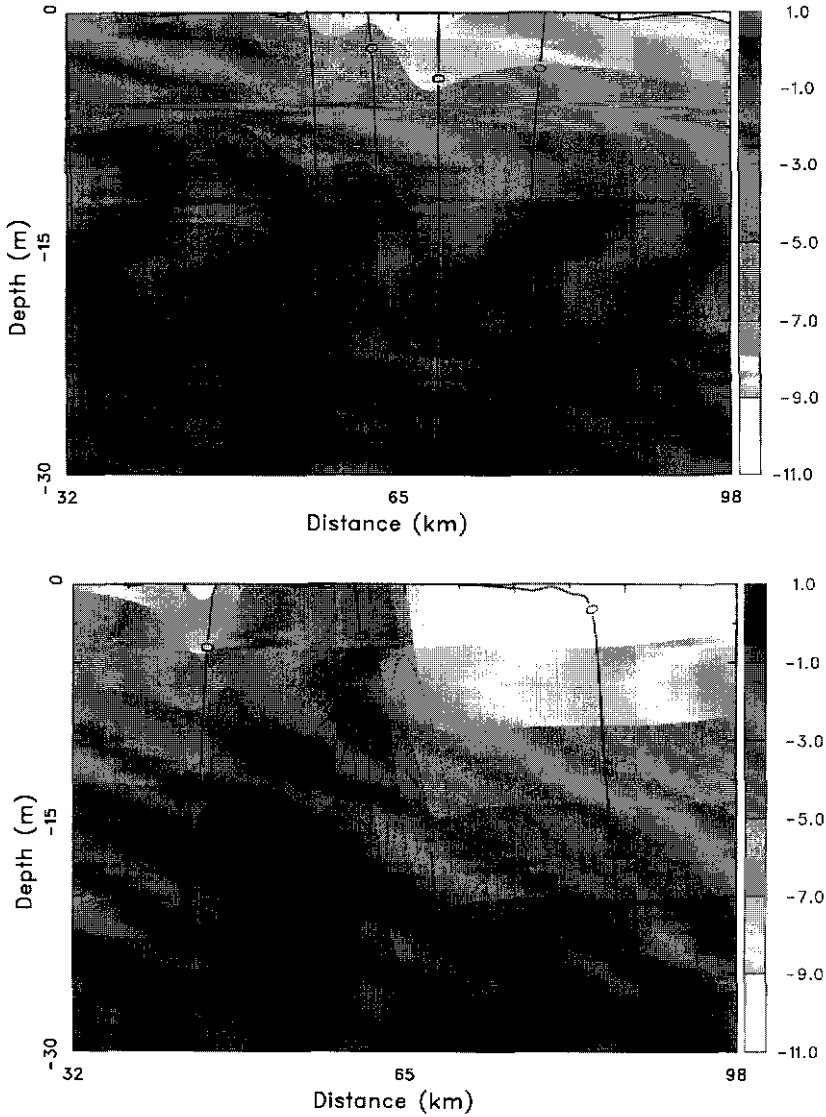
Figure 13
The vertical cross section of east–west current (cm s^{-1}) in gray scale and vertical velocity (cm s^{-1}) in contours along the line, $y = 37$ for the ocean in the coupled simulation for (a) 2 h and (b) 4 h. The vertical velocity has been multiplied by 10^3. The contour interval is then 2.0×10^3 cm s^{-1}. Only a subdomain, 32 to 98 km in x direction and 0 to 30 m in z direction, is shown to emphasize important features.
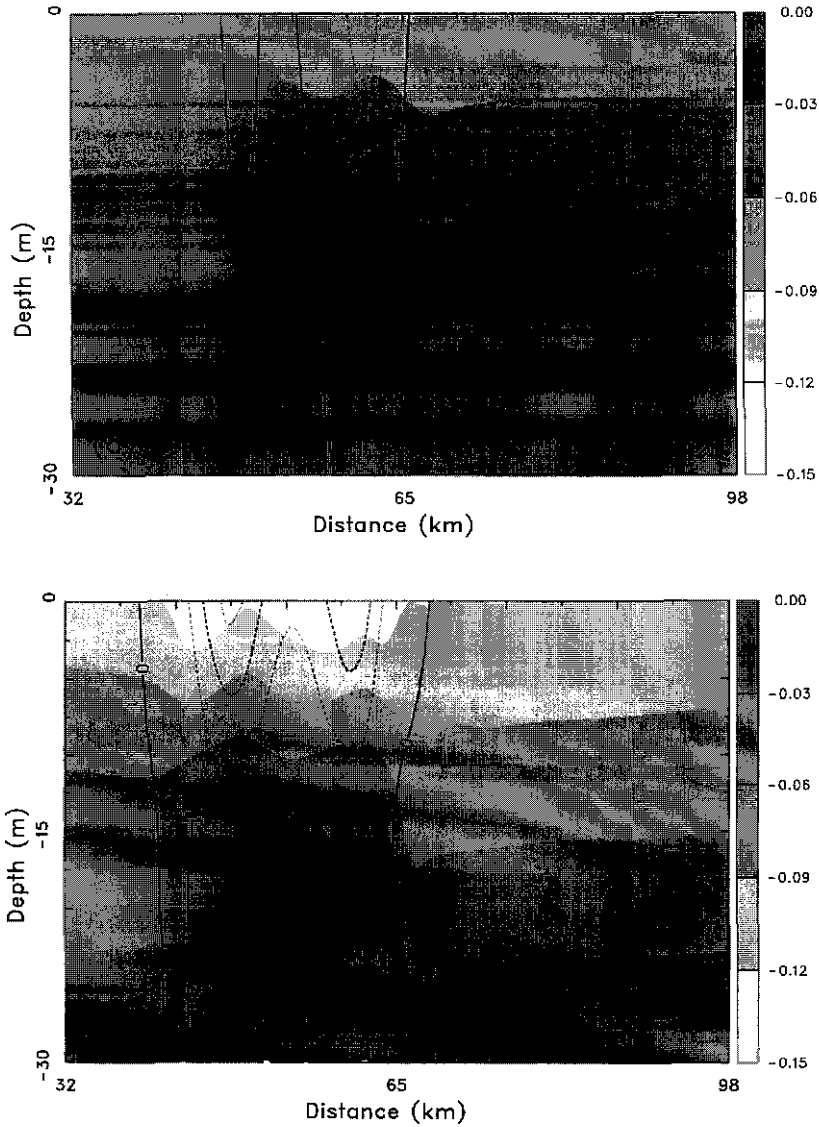
Figure 14
The vertical cross section of oceanic temperature change (°C) in gray scale and salinity change (ppt) in contours along the line, $y = 37$ in the coupled simulation for (a) 2 h and (b) 4 h. The contour interval is 0.1 ppt. Only a subdomain, 32 to 98 km in x direction and 0 to 30 m in z direction, is shown to emphasize important features.

current (cm s^{-1}) in gray scale and vertical velocity (cm s^{-1}) in contours for the ocean in the coupled simulation for 2 h and 4 h, respectively. Note that the vertical velocity in the ocean has been multiplied by 10^3 cm s^{-1} in Figure 13. During the early stages of the squall line (Figs. 12a and 13a), atmospheric convergence associated with the upward motion in the leading edge of the convective system causes upwelling in the ocean surface layer by Ekman transport. Similarly, divergent area in the atmospheric boundary layer causes downwelling in the ocean. The upwelling and the downwelling are small at this stage. The ocean current forced by the atmospheric wind stress contains a wave pattern in response to the updrafts and downdrafts in the atmosphere at different locations. Stronger easterly current in the right side of the figure is in response to strong wind stress near the leading edge of the squall line. Strong winds are associated with the inflow jet in the atmosphere (Fig. 6a). When the squall line intensifies (Fig. 12b), ocean current also becomes strong (Fig. 13b). The large upwelling area in the ocean is related to large upward motion in the atmosphere, as can be seen in the distribution of u and w components of the ocean current.

Initial warm SST increases the air temperature in the atmospheric surface layer, leading to an increase in instability and producing deep convection. Precipitation caused by the squall line cools the atmospheric surface layer and changes thermal fields in the ocean. Changes in the temperature and salinity in the ocean are evidenced in Figures 14a and b, which are the vertical cross sections of oceanic temperature change (°C) in gray scale and salinity change (ppt) in contours along the line, $y = 37$ in the coupled simulation for 2 h and 4 h, respectively. The effect of upwelling tends to raise the thermocline, bringing colder water in the deeper layer upwards.

Precipitation and the resulting freshwater flux from the atmosphere to the ocean appears to impact the dynamics of the ocean. Both temperature and salinity affect the mixed-layer depth. In the region where precipitation occurs, the mixed layer (as indicated approximately by the first thermocline) is relatively shallow because of the presence of freshwater (Fig. 14a). Lower temperature in the surface tends to destabilize the stratification and increases turbulent mixing. However the variation in salinity, created by a downward flux of freshwater, generates a distinct stable layer near the surface. The salinity gradient indicates lateral advection. This gradient increases as the squall line becomes stronger at 4 h (Fig. 14b), implying more freshwater flux downwards. Increased precipitation also cools the air temperature in the surface. Note that the horizontal temperature gradient has become weaker, meaning decreased SST in the coupled simulation in response to atmospheric forcing. Thermocline has risen significantly by strong upwelling, resulting in stronger horizontal temperature gradient in the deeper layer. The temperature and salinity gradients have also increased. The mixed layer is quite shallower in the area of precipitation comparable to other areas, implying that the stabilizing effect of the salinity gradient is dominant.

(4) Strength of the squall line

Coupled and uncoupled simulations appear to have an effect on the strength of the squall line. Figure 15 shows the difference of cloud water and rain water
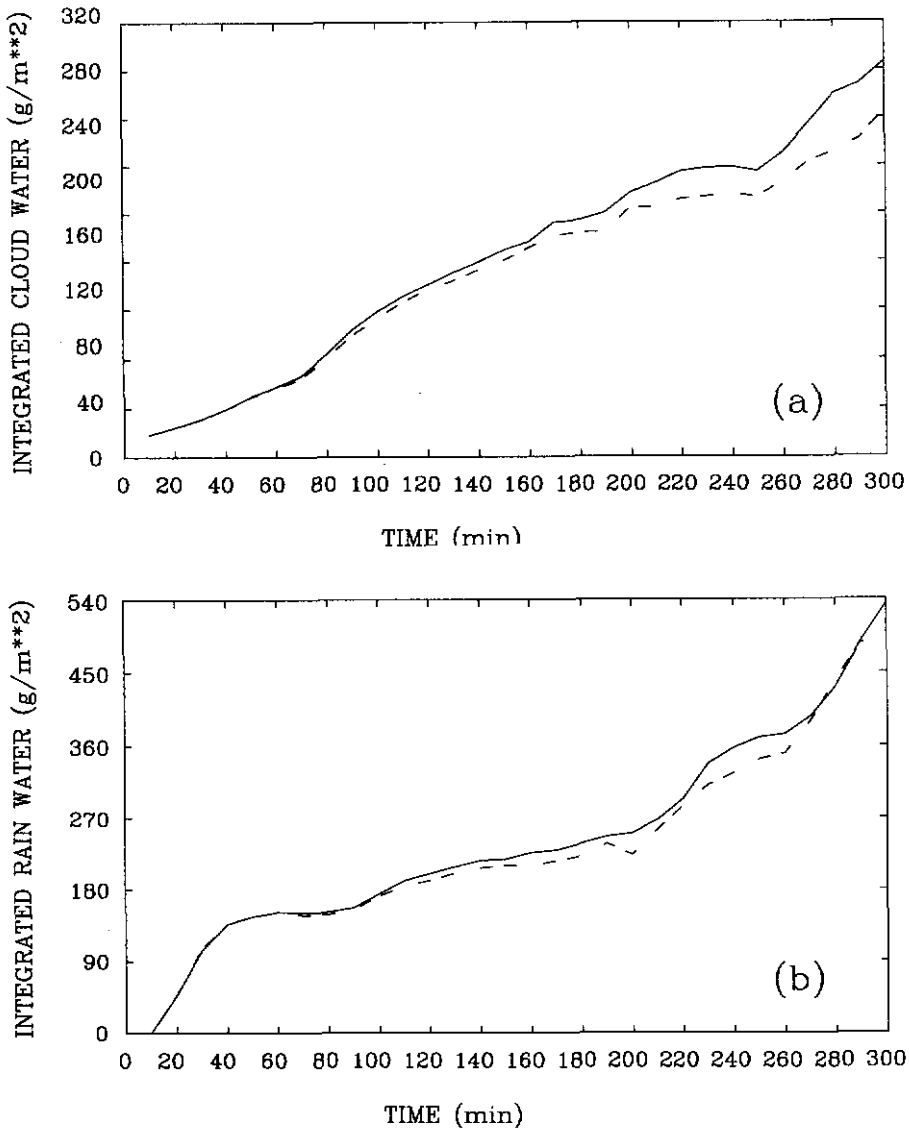

Figure 15

The time variation of vertically integrated, horizontally averaged (a) cloud water (g m^{-2}) and (b) rain water (g m^{-2}). The solid line and dashed line represent the uncoupled and coupled simulations, respectively.

between these two simulations. The values in the figures are vertically integrated and horizontally averaged. Cloud water from the coupled simulation is less than that from the uncoupled simulation. The maximum differences reach 10% for each variable. It is interesting to note that a slight deviation in the surface condition, such as the SST cooling, can produce a relatively substantial variation in the strength of the squall line. The predicted vertical velocities from both the simulations also indicate a significant difference in the circulations between the two simulations. This is obvious by comparing Figures 8 and 12. These two vertical cross sections are from the uncoupled and coupled simulations, respectively, with the same model location and simulation time. The maximum vertical velocity in the upper layer for the coupled simulation (4.97 m s^{-1} in Fig. 12b) is smaller than that for the uncoupled simulation (7.77 m s^{-1} in Fig. 8b). Weaker upward motion for the coupled simulation consequently produces less cloud water and rain water. However, the convective motion is stronger in the lower layer for the coupled simulation (5.56 m s^{-1} in Fig. 12b) than that for the uncoupled simulation (4.86 m s^{-1} in Fig. 8b). This results because cooler ocean surface at the leading edge of the squall line in the coupled simulation produces a stronger gust front and subsequently leads to a favorable condition for convective motion.

6. Conclusions

Coupled air–sea interaction processes associated with a squall line over the TOGA/COARE region are investigated employing the Coupled Ocean/Atmosphere Mesoscale Prediction System (COAMPS). Sensitivity studies were also conducted to determine the effect of coupling. The numerical model was initialized using TOGA/COARE observations of 22 February, 1993. A composite sounding using rawinsonde data and the P-3 flight level data was used for the atmosphere. CTD data from the SeaBird SBE-9 probe were used for the ocean.

The structure of the simulated squall line is close to the observations. Air is ingested into the squall line at low altitudes towards the rear of the squall line, which then accelerates upward. This leads to the formation of the main updraft with a rearward tilt with height. This structure is also consistent with the observations. A rear inflow jet develops beneath this front-to-rear flow. The counter-rotating vortices form, resulting in a bow-shape bulge towards the leading edge. The vortices include one counterclockwise on the northern or equatorward end of the line and one clockwise on the southern or poleward end of the line.

In addition to the above results, which were also shown in the previous numerical simulations (TRIER *et al.*, 1996, 1997), the unique results from the coupled simulation indicate that the air–sea interaction processes within the squall line are important. The results reveal the mechanisms of the exchanges of interfacial energy fluxes during the development of the squall line and its maintenance. The

increase in the sea-surface temperature (SST) is limited by the ingestion of cold freshwater into the ocean. Smaller SST decreases the instability in the atmospheric boundary layer, resulting in weaker convective motions. Both the dynamic and the thermodynamic structures of the ocean mixed layer are effected by the squall line through upwelling and baroclinicity. Temperature acts to destabilize the ocean mixed layer whereas salinity acts as a stabilizing factor. Feedback processes have little effect on surface sensible heat flux, although they do have an effect on the latent heat flux during the development of the squall line. The fluxes from the coupled simulation are about 10% less than that of the uncoupled simulation as the SST decreases by about 0.21°C in the coupled simulation. The squall line from the coupled simulation is somewhat weaker compared to the uncoupled simulation, according to the difference of cloud water, rain water and vertical velocity between the two simulations.

REFERENCES

BRANDES, A. E. (1990), *Evolution and Structure of the 6–7 May, 1985 Mesoscale Convective System and Associated Mesovortex*, Mon. Wea. Rev. *118*, 109–127.

CHANG, S. W. (1985), *Deep Ocean Response to Hurricanes as Revealed by an Ocean Model with Free Surface. Part I: Axisymmetric Case*, J. Phys. Oceanogr. *15*, 1847–1858.

CLANCY, R. M., and MARTIN, P. J. (1981), *Synoptic Forecasting of the Oceanic Mixed Layer Using the Navy's Operational Environmental Database: Present Capabilities and Future Applications*, Bull. Amer. Meteor. Soc. *62*, 770–784.

CLANCY, R. M., and POLLAK, K. D., *A real-time synoptic ocean thermal analysis/forecast system*. In *Progress in Oceanography*, Vol. 12 (Pergamon Press 1983) pp. 383–424.

DAVIS, C. A., and WEISMAN, M. L. (1994), *Balanced Dynamics of Simulated, Long-lived, Mesoscale Convective Systems*, J. Atmos. Sci. *51*, 2005–2030.

DEARDORFF, J. W. (1980), *Stratocumulus-capped Mixed Layers Derived from a Three-dimensional Model*, Bound.-Layer Meteor. *18*, 495–527.

GILL, A. E., *Atmosphere–Ocean Dynamics* (Academic Press 1982) 622 pp.

HARSHVARDHAN, R., DAVIES, RANDALL, D., and CORSETTI, T. (1987), *A Fast Radiation Parameterization for Atmospheric Circulation Models*, J. Geophys. Res. *92*, 1009–1015.

HODUR, R. M. (1997), *The Naval Research Laboratory's Coupled Ocean/Atmosphere Mesoscale Prediction System (COAMPS)*, Mon. Wea. Rev. *125*, 1414–1430.

HODUR, R. M. (1993), *Development and Testing of the Coupled Ocean/Atmosphere Mesoscale Prediction System (COAMPS)*, Naval Research Laboratory, Monterey, NRL/MR/7533-93-7213, 81 pp.

JOHNSON, R. H., and HAMILTON, P. J. (1988), *The Relationship of Surface Pressure Features to the Precipitation and Air Flow Structure of an Intense Midlatitude Squall Line*, Mon. Wea. Rev. *116*, 1444–1472.

JORGENSEN, D. P., LeMONE, M. A., and TRIER, S. B. (1997), *Structure and Evolution of the 22 February 1993 TOGA COARE Squall Line: Aircraft Observations of Precipitation, Circulation, and Surface Energy Fluxes*, J. Atmos. Sci. *54*, 1961–1985.

JORGENSEN, D. P., MATEJKA, T. J., and LeMONE, M. A. (1995), *Structure and Momentum Fluxes within a TOGA/COARE Squall Line System Observed by Airborne Doppler Radar*, Proceedings of 21st Conference on Hurricanes and Tropical Meteorology, Miami, Florida, pp. 579–581.

JORGENSEN, D. P., MATEJKA, T. J., JOHNSON, D., and LeMONE, M. A., *A TOGA/COARE Squall Line Seen by Multiple Airborne Doppler Radars*, Proceedings of Sixth Conference on Mesoscale Processes (Portland, Oregon 1994) pp. 25–28.

JORGENSEN, D. P., and SMULL, B. F. (1993), *Mesovortex Circulations Seen by Airborne Doppler Radar within a Bow-echo Mesoscale Convective System*, Bull. Am. Meteor. Soc. *74*, 2146–2157.

KAIN, J. S. (1990), *A One-dimensional Entraining–detraining Plume Model and its Application in Convective Parameterization*, J. Atmos. Sci. *47*, 2784–2802.

KAIN, J. S., and FRITSCH, J. M., *Convective parameterization for mesoscale models: The Kain-Fritsch scheme*. In *The Representation of Cumulus Convective in Numerical Models*, Meteor. Monogr., No. 46 (Amer. Meteor. Soc. 1993) pp. 165–170.

KLEMP, J., and WILHELMSON, R. (1978), *The Simulation of Three-dimensional Convective Storm Dynamics*. J. Atmos. Sci. *35*, 1070–1096.

LeMONE, M. A., JORGENSEN, D. P., and SMULL, B. F., *The Impact of Two Convective Systems on Sea-surface Stresses in COARE*, Proceedings of Sixth Conference on Mesoscale Processes (Portland, Oregon 1994) pp. 40–44.

LOUIS, J. F., TIEDTKE, M., and GELEYN, J. F. (1982), *A Short History of the Operational PBL-Parameterization at ECMWF*, Workshop on Planetary Boundary Parameterization, Reading, United Kingdom, ECMWF, 59–79.

MELLOR, G., and YAMADA, T. (1974), *A Hierarchy of Turbulence Closure Models for Planetary Boundary Layers*, J. Atmos. Sci. *31*, 1791–1806.

MILLER, M. J., and THORPE, A. J. (1981), *Radiation Conditions for the Lateral Boundaries of Limited-area Numerical Models*, Quart. J. Roy. Meteor. Soc. *107*, 615–628.

ORLANSKI, I. (1976), *A Simple Boundary Condition for Unbounded Hyperbolic Flows*, J. Comput. Phys. *21*, 251–269.

RUTLEDGE, S. A., and HOBBS, P. V. (1983), *The Mesoscale and Microscale Structure of Organization of Clouds and Precipitation in Midlatitude Cyclones. VIII: A Model for the "Seeder–feeder" Process in Warm-frontal Rainbands*, J. Atmos. Sci. *40*, 1185–1206.

SAUNDERS and FOFONOFF (1976), Deep-Sea Res. *23*, 109–111.

SMITH, P. L., Jr., MYERS, C. G., and ORVILLE, H. D. (1975), *Radar Reflectivity Factor Calculations in Numerical Cloud Models Using Bulk Parameterization of Precipitation Processes*, J. Appl. Meteor. *14*, 1156–1165.

TRIER, S. B., SKAMAROCK, W. C., LeMONE, M. A., PARSONS, D. B., and JORGENSEN, D. P. (1996), *Structure and Evolution of the 22 February 1993 TOGA COARE Squall Line: Numerical Simulations*, J. Atm. Sci. *53*, 2861–2886.

TRIER, S. B., SKAMAROCK, W. C., and LeMONE, M. A. (1997), *Structure and Evolution of the 22 February, 1993 TOGA COARE Squall Line: Organization Mechanisms Inferred from Numerical Simulation*, J. Atm. Sci. *54*, 386–407.

WEBSTER, P. J., and LUKAS, R. (1992), *TOGA COARE: The Coupled Ocean–atmosphere Response Experiment*, Bull. Am. Meteor. Soc. *73*, 1377–1416.

WEISMAN, M. L., KLEMP, J. B., and ROTUNNO, R. (1988), *Structure and Evolution of Numerically Simulated Squall Lines*, J. Atmos. Sci. *45*, 1990–2013.

WEISMAN, M. L. (1993), *The Genesis of Long-lived Bow Echoes*, J. Atmos. Sci. *50*, 645–670.

XU, L. (1995), *The Study of Mesoscale Land–air–sea Interaction Processes Using a Nonhydrostatic Model*, Ph.D. Dissertation, North Carolina State University, Raleigh, 336 pp.